Slow-Rise and Fast-Rise Phases of an Erupting Solar Filament, and Flare Emission Onset

Alphonse C. Sterling and Ronald L. Moore

NASA/Marshall Space Flight Center,
XD12/Space Science Branch, Huntsville, AL 35812
alphonse.sterling@nasa.gov
ron.moore@nasa.gov

To appear in The Astrophysical Journal
(Accepted: May 20, 2005)

ABSTRACT

We observe the eruption of an active-region solar filament of 1998 July 11 using high time cadence and high spatial resolution EUV observations from the *TRACE* satellite, along with soft X-ray images from the soft X-ray telescope (SXT) on the *Yohkoh* satellite, hard X-ray fluxes from the BATSE instrument on the Compton Gamma Ray Observatory (*CGRO*) satellite and from the hard X-ray telescope (HXT) on *Yohkoh*, and ground-based magnetograms. We concentrate on the initiation of the eruption in an effort to understand the eruption mechanism. Prior to eruption the filament undergoes slow upward movement in a "slow rise" phase with an approximately constant velocity of $\approx$ 15 km s^{-1} that lasts about 10 min. It then erupts in a "fast-rise" phase, accelerating to a velocity of $\approx$ 200 km s^{-1} in about 5 min, and then decelerating to $\approx$ 150 km s^{-1} over the next 5 min. EUV brightenings begin about concurrent with the start of the filament's slow rise, and remain immediately beneath the rising filament during the slow rise; initial soft X-ray brightenings occur at about the same time and location. Strong hard X-ray emission begins after the onset of the fast rise, and does not peak until the filament has traveled to a substantial altitude (to a height about equal to the initial length of the erupting filament) beyond its initial location. Our observations are consistent with the slow-rise phase of the eruption resulting from the onset of "tether cutting" reconnection between magnetic fields beneath the filament, and the fast rise resulting from an explosive increase in the reconnection rate or by catastrophic destabilization of the overlying filament-carrying fields. About two days prior to the event new flux emerged near the location of the initial brightenings, and this recently-emerged flux could have been a catalyst for initiating the tether-cutting reconnection. With the exception of the sudden transition from the slow-rise phase to the fast-rise phase in our event, our filament's height-time profile is qualitatively similar to the erupting-flux-rope height as a function of time computed by Chen & Shibata (2000), for a model in which the eruption is triggered by reconnection between emerging field and other field under the flux rope.

Subject headings: Sun: flares — Sun: filaments — Sun: UV radiation — Sun: X-rays, gamma rays — Sun: coronal mass ejections (CMEs)

1. Introduction

Solar filament eruptions are one aspect of a more general magnetic eruption that can produce solar flares and coronal mass ejections (CMEs). Filaments are chromospheric material suspended in the corona by magnetic fields; these fields and the entrained filament material erupt together (e.g., Rust 1976). Since we cannot see the erupting fields themselves, filaments can be useful tracers of the locations and movements of the erupting fields. Recently we have been using filament motions to study the earliest stages of eruptions, in an effort to gain greater understanding of the eruption-onset mechanism (Sterling & Moore 2003, 2004a, 2004b). Those previous studies examined four different filament eruptions in detail, and all of the studies were based on images from the Extreme-Ultraviolet (EUV) Imaging Telescope (EIT) on *SOHO*. In each case the eruption involved large-scale quiet-region filaments, and each eruption began with a relatively slow rise of the filament (slow-rise phase), followed by a transition to a more-rapid acceleration phase (fast-rise phase), and we call the transition from the slow-rise to the fast-rise the eruption onset. Sterling & Moore (2004b) show

examples where larger coronal cavities containing the filaments are apparent, and that the cavities themselves also take part in the two-phase evolution. Therefore we infer that the two-phase evolution is a key dynamical aspect of the entire set of erupting fields, and not of the filaments alone.

In this paper we present our first detailed study of an active region filament eruption, and our first based on *TRACE* images. EIT has relatively course time cadence of about 12 min, while *TRACE* observations in a given filter are at a cadence of 1 min or less, and *TRACE* also has better spatial resolution than EIT (about $1''$ compared to $5''$). Alas, EIT observes the entire Sun while *TRACE* has a limited field of view (FOV) and so many filament eruptions are missed by *TRACE*, but the event of 1998 July 11 discussed here occurs completely within the *TRACE* FOV. With the insight gained from our studies of EIT events, we examine the higher-cadence and higher-resolution *TRACE* data to address the question of the mechanism of the eruption onset and the details of the slow-rise phase for this event.

2. Instrumentation and Data

Our primary data are images from *TRACE*, taken with both the 195 Å Fe XII filter and the 1600 Å UV filter. Images in Fe XII nominally show cooler corona, being most sensitive to emissions of 1.5 MK, although the 195 Å bandpass also includes contributions from the Fe XXIV line at 192 Å that are significant when the emitting plasmas are hotter than about 15 MK. Images from the 1600 Å filter generally show features near the level of the photosphere, with C IV emission from loops and ribbons during flares. Handy et al. (1998) give details of the *TRACE* instrument. We also use images from the soft X-ray telescope (SXT) on *Yohkoh* (Tsuneta et al. 1991), hard X-ray data from the BATSE instrument (DISCLA channel 1 data; Fishman et al. 1989, Harmon et al. 1989) on the Compton Gamma Ray Observatory (*CGRO*) and from the L channel (13.9 — 22.7 keV) of the Hard X-ray Telescope (HXT) on *Yohkoh* (Kosugi et al. 1991), and magnetic field data from Kitt Peak longitudinal magnetograms. *SOHO* data are not available during the period of this event due to technical difficulties with the satellite.

Our filament eruption occurred on 1998 July 11 and was accompanied by soft X-ray flux peaking at 04:41 UT at a *GOES* level of C1.7, and occurred near the southwest limb at solar coordinates (700, -450). We use *TRACE* 195 Å images from 04:10 UT until 04:55 UT with a 1024-pixel square FOV ($512'' \times 512''$) at about 30 s cadence, and we use *TRACE* 1600 Å images over the same time period with 512-pixel square FOV ($256'' \times 256''$) also at about 30 s cadence.

3. Observations and Analysis

3.0.1. Morphology

Figure 1 shows the morphology of the erupting region in 195 Å images, with boxes surrounding areas of interest from which we will derive lightcurves below. In (a) the top of the filament that erupts is in box 2, while the filament top is just beyond the northwest corner of box 2 in (b); as we will show in Figure 3 below, this shift in position results from the slow rise of the filament. Also in (b), there is brightening under the rising filament. By Figure 1c, the filament fast-phase eruption has begun and its top reaches the northwest corner of box 1, while the filament is well beyond box 1 in (d).

Figure 2 shows 1600 Å images at times corresponding to those of Figure 1. Comparing Figures 2a and 2b shows that a weak brightening appears in box 2 during the time of the filament's slow rise. By the time of Figure 2c, box 2 and surrounding areas in box 1 contain bright flare ribbons. Box 3 shows brightening at a distant location beginning in Figure 2c.

3.0.2. Evolution in Time

Figure 3a shows the projected displacement of the filament in the plane of Figure 1 (which we call the filament height) as a function of time, along with its velocity and acceleration. As with our previous studies, the filament height shows a slow-rise phase followed by a fast-rise phase. In the figure the slow rise is obvious between about 04:22 and 04:30 UT, although inspection of a movie made from the *TRACE* images shows that the slow rise, or at least an agitation of the filament (filament activation), was underway even when observations started at 04:10 UT. Roughness in the trajectory between about 4:27 UT and 4:31 UT appears to be due to rapid filament motions (perhaps shaking or unwinding), but could instead be due to selective fading of some parts of the filament. A qualitative change in the evolution begins with onset of the fast-rise phase at about 04:31 UT. In addition to the height profile, the derived velocity shows two phases of evolution. Estimating the velocity directly from the height curve using a two-point linear extrapolation between 04:22:35 and 04:31:07 UT gives 14.4 km s^{-1}, and this agrees with the values indicated by the calculated velocity curve in Figure 3a. During the fast-rise phase the velocity reaches a maximum of $\approx$ 200 km s^{-1} near 04:36 UT, and decreases to about 150 km s^{-1} in about 5 min, and continues to decrease at a slower rate after that.

Hard X-rays from BATSE, also plotted in Figure 3a, show a substantial increase above background beginning at 04:33 UT, which is 2 to 3 min after our estimate of the time of the fast-rise phase onset. We also show fluxes from the L channel of HXT on *Yohkoh*, and these indicate that there is no substantial HXR burst activity between 04:10 and about 04:32 UT, at which time the HXT data end due to *Yohkoh* entering satellite night. These HXT fluxes do show a gradual increasing trend in the flux from about 04:29 UT or perhaps earlier, but this is more likely from leakage of thermal soft X-ray emission into the hard X-ray passband than from non-thermal hard X-ray emission. Hence, the hard X-ray burst probably began after 04:32 UT. The steepest rise in filament velocity (strongest acceleration) coincides with onset and rise of the hard X-ray burst to its peak.

Figure 3b shows *TRACE* 195 Å and 1600 Å intensity lightcurves derived from the boxed locations of Figures 1 and 2. Lightcurves for box 1 represent the entire main flaring region, and show an initial ("preflare") brightening peaking just before 04:24 UT followed by onset of the main flare brightening at about 04:31 UT; the ramp-up of the intensity of this preflare brightening begins prior to 04:19 UT with even earlier flickering (based on inspection of intensity difference images), and therefore the brightening is concurrent with the start of the filament's slow rise within our detectability limit. In addition to capturing the preflare brightening, box 1 also includes brightenings of the flare ribbons starting about concurrent with onset of the main flare at about 04:31 UT. The lightcurve for box 3 shows weak intensity increases remote from the main erupting filament from about 04:26 UT, and in a movie made from the *TRACE* images this corresponds to activation of a thin filament located in that region; these brightenings have a steep rise beginning after the start of the steep intensity rise of the main flaring region (box 1). From the movies, both the pre-eruption and the eruption box 3 brightenings appear to be in response to activity of the main filament; that is, the weak and strong box 3 brightenings appear to be triggered respectively by the slow- and fast-rise phase activity of

the main filament. Through the time of the first bright intensity peak, lasting until about 04:37 UT, the 195 Å and 1600 Å lightcurves for each box closely track each other.

We have four usable (i.e., without intensity saturation, etc.) soft X-ray images from SXT near eruption time; they were taken with the AlMg filter at 04:07:10, 04:15:34, 04:24:06, and 04:32:44 UT on 1998 July 11. After this last image *Yohkoh* entered satellite night. As the exposure duration is very short (38 msec) and the spatial resolution coarse (4″.91), the quality of these images is not high (Fig. 4d), with several pixels in box 4 not registering a positive flux. Nonetheless these images are adequate for seeing soft X-ray intensity changes in various parts of the active region as the eruption starts. Figure 3b includes four stars that represent the ratio of the intensity of flux in SXT AlMg-filter images at the location of box 2 to the intensity of the rest of the active region, where "the rest of the active region" consists of the intensity sums of boxes 1, 3, and 5, minus the intensity of box 2, where box 5 is as shown in Figure 4d, and where boxes 1 through 4 are the same as in Figures 1 and 2. These SXT intensities show a relatively constant flux level over the two earliest times, followed by an intensity increase at the location of box 2 at the start of the most obvious slow rise phase, coinciding with the *TRACE* intensity peak in the slow-rise phase. At the time of the final SXT point the box 2 region is flaring, resulting in a dramatic soft X-ray intensity enhancement at the location of box 2. In contrast, the soft X-ray intensity in parts of the active region other than box 2 remains about constant compared to the background (which we take to be the summed flux of box 4) over this time period; for the three points between 04:07 and 04:24 UT, this ratio is within 0.05 in the log, and for all four points the ratio is within 0.3 in the log, where some of the scatter may result from the zero-intensity level of some of the box 4 pixels.

We say that the filament "erupts" from about 04:31 UT when it begins to accelerate, although due to the absence of *SOHO* LASCO data we cannot say with certainty whether the filament fully escapes from the Sun as part of a CME. As mentioned above, this transition in filament velocity is nearly concurrent with the EUV intensity rise in box 1. Later in the event additional brightenings occur around 04:42 UT in boxes 1 and 2. These are due to brightening of a low-lying (near the site of box 2) post-eruption flare loop, which appears not to involve ejection of additional material; we believe that these are post-flare loops that become visible in EUV as they cool from flare temperatures. Figure 3b shows that at these times (later than about 04:40 UT) the 195 Å channel emission dominates the 1600 Å emission in boxes 1 and 2, indicating a higher ratio of coronal emission to footpoint C IV emission at the locations encompassed by box 1; this is consistent with these loops cooling in the post-flare phase.

3.1. Magnetic Geometry

Figure 4 shows the magnetic arrangement of the erupting region. Figure 4a shows a Kitt Peak magnetogram from 2004 July 9, with contours identifying locations of weaker and stronger magnetic field. Figures 4b — 4d show these same contours overlaid onto *TRACE* 195 Å, *TRACE* 1600 Å, and SXT images, respectively. We have rotated the magnetogram, which was taken approximately 35 hrs prior to the eruption, to register it with the erupting region. A magnetogram from July 10 (the day prior to the eruption) is also available, but due to the region's proximity to the limb it is more subject to false field values than is the magnetogram we use. Even the magnetogram of Figure 4 has some false values due to projection effects near the limb, but we believe that with it, along and with the help of earlier magnetograms from when the region was closer to disk center (e.g., July 8), we can reliably identify key magnetic features of the region. Overall, the negative spot (arrow 1 in Fig. 4c) is

surrounded to the south by strong positive flux, and to the east and the north by weaker positive flux; we suspect that some of the flux northwest of the spot that appears weakly negative in Figure 4a is actually weakly positive, and only appears negative due to projection. Therefore, overall we believe that the negative spot is surrounded on the south, east, and north by positive flux, and this implies that there is a neutral line running on these sides of the negative spot; the surrounding positive flux includes the flux concentrations identified by arrows 4, 5, and 6 in Figure 4c. Comparing features in the *TRACE* images with weaker areas of concentrated field suggests that our Kitt Peak-*TRACE* overlays are aligned to within ~ 5 arcsec over most of the field of view of the images, although there could have been some evolution in the field that we cannot identify over the 35 hrs between the time of the magnetogram and the eruption. Alignment accuracy of the magnetogram with the SXT image in Figure 4d seems to be similar to that with the *TRACE* images, within the limitations of the much-more-coarse resolution of the SXT image.

Arrows 2 and 3 of Figure 4c indicate a strong and compact bipole not prominent in a Kitt Peak magnetogram from the previous day, and therefore we take it to be an emerging flux region (also shown in Fig. 5 below). This emerging flux is very close to or at the location of box 2, where the filament resides and the eruption begins, and this is where we see the first brightening near 04:24 UT (Fig. 4b). In Figure 4c the positive end of this bipole is at the edge of one of the ribbons of the flare during the eruption. Therefore, we suspect that this emerging flux was a primary factor in the eruption onset, even though it would have undergone some evolution between the time of emergence and the time of the eruption.

Figure 4c is close in time to Figure 2c, and brightenings visible in Figure 2c occurring in the lower portion of box 3 are rooted in areas of largely positive magnetic flux indicated by arrow 7 in Figure 4c.

3.2. Slow-Rise Phase, and Transition to Fast Rise Phase

Figures 5 and 6 show the erupting region in more detail. Figures 5a through 5c show 1600 Å images of the region during the time of the filament's slow-rise phase. Figure 5b shows a mound-like structure, most of it fitting inside the white box of that image (which is the same as box 2 in Figs. 1 and 2). This feature grows in time, although some parts of it begin to fade by the time of Figure 5c, corresponding to a drop in intensity of lightcurves 1 and 2 of Figure 3b. In Figure 5d, at the start of the fast-rise phase, it has nearly faded out, but a feature on its north side becomes visible and begins to grow. By the time of Figure 5e, the filament's fast-rise phase is in progress, and the flare is underway. We can identify at least six flare ribbons, indicated by arrows in Figure 5e, and these ribbons have spread further apart and become less-distinct by the time of Figure 5f. Figures 5c and 5f include the magnetogram of Figure 4 overlaid on the *TRACE* images, showing that the emerging flux region (arrows 2 and 3) occurred in the immediate vicinity of the erupting filament and flare ribbons.

Figure 6 shows images in 195 Å at corresponding times. During the slow-rise phase time period (Figs. 6a—6c), the brightening is concentrated below the rising filament. Flare ribbons are identifiable in Figure 6e, after the filament's fast rise is underway.

These observations have implications for the filament's slow-rise phase. As mentioned earlier, down to the limits of detectability the onset of the slow-rise phase begins about concurrent with the start of the preflare brightening in boxes 1 and 2, and Figure 6 shows that this brightening appears

to reside beneath the filament that erupts; this suggests that the dynamical activity associated with the preflare brightening could be a driver of the filament's slow rise. Between the times of the preflare brightening peak near 04:24 UT and the main flare brightening near 04:31 UT the intensity in the preflare-brightening location (including most of box 2) never drops back to its values prior to preflare-brightening onset (i.e. prior to about 04:19 UT). Figure 6c shows that the brightening becomes weaker and more dispersed in the 195 Å image during this time period; this is probably due to cooling rather than heating, since the 1600 Å C IV emission also fades during this time (heating of flare loops to temperatures $> 1.5 \times 10^6$ K would lead to increased heat conduction to the transition region, and corresponding brightening in 1600 Å).

3.3. Eruption Mechanism — Speculations

In our earlier studies we have tried to identify which theoretical model for eruptions best fits our observations. We have concentrated on two specific eruption mechanisms. One of these is the "tether cutting" mechanism (Moore & Labonte 1980, Sturrock 1989, Moore & Roumeliotis 1992, Moore et al. 2001), according to which eruption occurs when highly-sheared fields in the core of a magnetic bipole reconnect, perhaps slowly at first, but then rapidly (runaway reconnection), explosively releasing the energy stored in the sheared fields, resulting in the eruption. The other mechanism we have focused on is "breakout" (Antiochos (1998) and Antiochos et al. 1999), according to which two or more bipoles are required for eruption, where one bipole pushes up into an overlying bipole leading to slow reconnection far from the core of the inner bipole (e.g., high in the corona) at a magnetic null point between the two bipoles. According to breakout, if this null-point reconnection is initially slow enough then great stress can build up between the two bipoles, and an explosive eruption can occur when this null-point reconnection becomes rapid.

For the event considered here, our observations indicate that magnetic reconnection below the filament releases the eruption, and this is consistent with some form of tether cutting. Our observations are not consistent with breakout, because the overall field configuration is bipolar and there is no flare brightening far from the neutral line prior to eruption. Details of this tether cutting, however, are uncertain because of the limitation of the magnetic field data, which are due to the region's proximity to the limb and the time-lag between the magnetogram and the event. From Figure 4, however, we can see the likely basic magnetic features of the region, and we know that newly-emerging flux appeared at the eruption site about two days prior to the event. Also, the location of the flaring ribbons in Figure 5e reflect the magnetic structure, since we expect expanding ribbons to reside on either side of a magnetic inversion line. From this information we infer that the likely magnetic configuration of the erupting region is as depicted in Figure 7. In this schematic, both the preflare brightening and the brightening of the flare itself occurs near the location of the newly-emerged flux, which is near where the neutral line kinks in the schematic.

Based on our observations and the schematic of Figure 7, we can make some speculations as to the cause of the eruption. Because the preflare brightening near 04:24 UT emits in soft X-rays (Fig 3b), we suspect that energy release via magnetic reconnection is occurring close to the site of the emerging flux; one possibility is that this reconnection is between a magnetic loop linking locations R2 and R3 (blue loop in Fig. 7), and a second loop linking locations R1 and R4 (red loop). This reconnection perhaps involves or is abetted by the newly-emerged flux. At the location where these loops cross, the vertical component of the field of the two loops are oppositely directed, allowing cancelation via reconnection. This reconnection results in loops connecting locations R1 and R2 (solid green loop),

which are at the location of the brightenings we see during the slow-rise phase of the filament most prominently in Figures 5b, 5c, 6b, and 6c. The reconnection also produces the dashed green loop connecting locations R3 and R4; this loop is part of the field traced by the rising filament. The sketch shows only two green loops, but in fact there would be a continuum of such loops created as arcades of blue and red loops reconnect. Fields represented by the dashed green line have less tension than the blue and red fields (that is, the tethers holding down the red and blue fields are reduced via tether cutting; e.g., Moore & Roumeliotis 1992), and so the upper product of the reconnection (the dashed green loop) bulges out farther from the surface and leads to expansion of the entire flux envelope that contains the filament (Loop 1), resulting in the slow rise of the filament. We are not certain of exactly how the transition to fast eruption takes place. One possibility is that the rate of tether-cutting reconnection becomes much faster after the filament flux rope has arched beyond some critical amount so that the eruption becomes explosive. Alternatively, formation of enough dashed-green-line-type fields via tether-cutting reconnection could have deformed the overlying field (that containing Loop 1) enough for an ideal magnetic instability or loss of equilibrium to ensue after exceeding some critical altitude, resulting in the explosive eruption. The field containing Loop 1 is sheared (as the presence of the filament indicates), and this would be a factor in its going unstable if deformed by a field pushing upward from below.

This activity leading to the onset of slow and fast eruption in the complex around Loop 1 could have disrupted Loop 2 (perhaps via reconnection between loops 1 and 2), and this would produce brightenings in the southern end of Loop 2, leading to the brightenings in box 3 of Figures 1 and 2.

4. Discussion

We have found that the filament eruption of 1998 July 11 is similar to larger-scale and more-slowly-evolving quiet region filament eruptions we have observed previously, in that there is an initial slow-rise phase followed by a fast-rise phase of the eruption (Sterling & Moore 2003, 2004a, 2004b). Due to the high time cadence of the *TRACE* data we are able to resolve the slow rise for this relatively fast-evolving active region eruption; our previous studies relied on EIT data with 12 min time cadence, which is why we could time-resolve the slow-rise phase in only more slowly-evolving quiet region eruptions. Pre-eruption slow-rise phases of filaments have been seen earlier also (e.g., Tandberg-Hanssen et al. 1980), and so the slow-rises are a common (but not universal, see Kahler et al. 1988) phenomenon. In the two events studied by Sterling & Moore (2004b), the magnetic cavity containing the filament was discernible, and they found that the slow filament rise was associated with a more general rise of the magnetic cavity; that is, the magnetic cavity rose slowly before being violently expelled from the Sun, and the filament "went along for the ride." We suspect that this is a common scenario, but non-filament portions of the cavity are often not apparent.

For many filaments then, the slow-rise seems to be a critical feature of their evolution toward eruption. Two questions are: What leads to the initial slow-rise, and what causes the transition from slow-rise to fast-rise? Regarding the slow-rise of the specific event considered here, within our detectability limits, preflare brightening and onset of the filament's slow-rise phase occurred in step with each other, and so it is plausible that the mechanism leading to the preflare brightening caused the filament to begin its upward movement. We have speculated that both the brightening and the slow rise could result from magnetic reconnection among highly-sheared magnetic loops below the filament, and this reconnection could have involved or been encouraged by a new flux system that emerged about two days earlier in the vicinity of the slow-phase brightenings. Transition to

the fast-rise phase would occur when the low-lying reconnection that initiated the slow-rise phase inflated the overlying filament-carrying fields enough so that they became unstable and violently erupted, perhaps due to an MHD instability or due to runaway tether cutting. Our magnetic data are not complete enough to examine this possibility satisfactorily, but such a sequence of events would heat the plasma, leading to the brightening, and explain the slow-rise and the fast-rise of the filament. As discussed above, this scenario is similar to the tether cutting picture described by Moore & Roumeliotis (1992). It is also similar to the model proposed by Heyvaerts, Priest, & Rust (1977), and to the scenarios modeled numerically by Chen & Shibata (2000) and Lin, Forbes & Isenberg (2001).

We must add, however, that we do not know how common it is for pre-eruption brightenings to accompany the start of the slow-rise phase, or how frequently any such brightenings are located beneath the erupting filament. SXT images of the six eruptions of sheared core fields in single-bipole configurations presented in Moore et al. (2001), however, do show similar brightening low in the sheared core field in the slow onset of each eruption. We did not observe such a pre-eruption EUV feature in the core region in our studies of slower events using EIT data, but this could have been due to poor time cadence and weaker magnetic fields. Studies of more eruptions using *TRACE* data are needed to address these questions.

Comparison with theory could help better determine the nature of the onset mechanism. In order to facilitate comparison between our observations and predictions of various numerical models, we can recast the filament height as a function of time in terms of normalized dimensionless units. We base our normalization on the Alfven transit time, τ_A, of the system. To estimate these parameters, we consider only the region in the immediate vicinity of the erupting filament. We measure an average value for the magnetic field strength, B, for a rectangular region in the images of Figure 4 approximately covering $810'' — 845''$ along the abscissa and $-330'' — -345''$ along the ordinate (this is the area of the southern-half of box 2 of Figure 4d, shifted southward by $5''$), and find a value of about 60 G. We take this value to be representative of the strength of the field that threads the filament before it erupts, that is, the initial field strength of the "flux rope" in which the erupting filament rides. Using a coronal density, ρ, of 2×10^{-14} g cm^{-3}, appropriate for an active region loop, gives an Alfven speed, $V_A = B/(4\pi\rho)^{1/2}$, of 1200 km s^{-1}. From Figure 1b, we measure the footpoint separation of the base of the erupting filament to be $\approx$ 25,000 km, which we take to be the Alfven scale length, L_A, of the system; these values yield $\tau_A \approx 21$ s. Figure 8 shows the filament trajectory of Figure 3a, with the filament height normalized to L_A and the elapsed time, t, normalized to τ_A. The Alfven speed could be somewhat (probably less than a factor of 2) slower around the time of eruption, as the average B may have reduced as the emerging flux dispersed over time.

We can compare our filament rise trajectory of Figure 8 with the rise trajectory predicted for an erupting flux rope by the model of Chen & Shibata (2000) shown in Figure 9. Their model is a two-dimensional magnetohydrodynamic (MHD) numerical simulation of the interaction of an emerging bipole and an arcade field encasing a flux rope situated along a filament channel. They find that the emerging bipole field cancels magnetic field below the flux rope, leading to the rise of the flux rope. Figure 9 is for their case where the emerging bipole is centered on the neutral line below the flux rope (their case A). They plot the reconnection rate, which we do not estimate. Instead, we plot the BATSE hard X-ray flux; we expect the hard X-ray flux profile to mimic the reconnection rate profile closely, since the current understanding of flares indicates that the hard X-rays result from non-thermal particles produced by the reconnection. Their reconnection lasts an order-of-magnitude longer duration than our hard X-ray burst (based on the detectable duration

of the burst), and over the duration of their strong reconnection their flux rope rises about three times the height that our filament rises over the time of our enhanced hard X-rays. Other differences between the two cases are assumptions about density (they assume $\rho = 10^{-15}$ g cm^{-3}) and differing length scales (they use $L = 10^5$ km). Despite these scale differences, from about time t/τ_A= 60, our rise curve is qualitatively similar to that in the simulation by Chen & Shibata. Prior to that time, however, our findings differ from that of the Chen & Shibata model in that their model predicts a smooth rise of the filament, while our observations show the filament's slow rise occurring between time t/τ_A of about $\lesssim$35 and 60. It is not clear yet how fundamental a difference this is, or whether a modification of parameters in the Chen & Shibata model or a three-dimensional geometry could provide a better match with our observations. Also, it is not yet known how common the slow rise is for erupting filaments, although such a slow rise is not uncommon, as discussed in §1.

For an event that evolved much more slowly than the present one, Sterling & Moore (2004b) found that a detectable hard X-ray burst occurred well after the start of the onset of the fast-rise phase. Figure 3 indicates that the fast rise begins before the detectable start of the hard X-ray burst in this case also, but the time delay is much reduced from the case of Sterling & Moore (2004b), who studied a quiet region filament eruption with one end of the filament in an active region; the hard X-rays were produced in the strong field in the active region, presumably when the eruption produced a current sheet in that field. The present eruption occurred entirely in an active region; we find that the peak of the hard X-ray burst occurs when the fast rise is well underway. Chen & Shibata also found that the peak of the reconnection rate was delayed from the start of the flux rope ejection, and that this peak is close to the maximum acceleration phase of the flux rope. Our observations indicate that the hard X-ray peak occurs toward the end of the phase of the strongest filament acceleration, and this seems to be similar to the Chen & Shibata results (although they follow the flux rope rather than a filament). It remains to be seen whether other eruption models could fit the observations equally well or better.

One possible explanation for this delay in our observations is that the internal reconnection that leads to the hard X-rays becomes more efficient as the filament rises: Initially the low-lying fields are nearly horizontal to the solar surface, and the oppositely-directed vertical components of the reconnecting field is relatively small. As the eruption progresses, the field beneath the rising filament becomes more vertical, and hence the oppositely-directed vertical components become larger; this could result in more rapid reconnection and the strong hard X-ray burst. That is, the three-dimensional nature of the eruption could be a factor in the delay of the peak of the hard X-ray burst. Figure 7 shows that the hard X-rays commence when the ratio of the filament height to the Alfven scale height is ≈ 0.5, and they peak when this ratio is > 1. That is, the hard X-ray burst did not begin until the filament had arched to a height comparable to its original length.

Figures 3b and 4d show that the pre-eruption brightening at about 04:24 UT has emission in soft X-rays. There have been many observations of soft X-ray emission prior to the onset of hard X-rays (e.g., Tanaka & Zirin 1985, Sterling et al. 1997, Alexander et al. 1998), with Harrison (1986) suggesting explicitly that an early brightening accompanies the launch of a coronal mass ejection (CME) and precedes a more-intense flare; our observations for this event are consistent with Harrison's view. We find the pre-eruption brightenings to be very near the location where the main flare begins; that is, near the highly-sheared core fields at the heart of the eruption-associated energy-release site. Sterling & Moore (2004b) also found pre-hard-X-ray-burst soft X-ray brightenings at the sheared core field location for an event, although their data were not complete enough to say whether the soft X-rays occurred during the latter part of the slow-rise phase or the early part of the fast-rise

phase of that filament eruption. Zhang et al. (2001) also discuss a period of pre-eruption soft X-ray intensity enhancement, which they termed the "initiation phase" of CME eruption; this seems to be closely associated with or identical to our filament slow-rise phase and associated enhancements in EUV and soft X-rays.

Our observations show an acceleration of the filament from the time of fast-rise onset at 04:31 UT until 04:36 UT, after which time it decelerates (velocity curve in Fig. 3a). In the *TRACE* 195 Å movie, the erupting structure loses its coherence and slows down during the deceleration period. Maximum velocity occurs about a minute (corresponding to a few τ_A in Fig. 8) after the end of the main hard X-ray peak. A similar deceleration also appears in Figure 9 from the Chen & Shibata (2000) model. This is also similar to the finding of Zhang et al. (2001) that CMEs observed with LASCO undergo an acceleration phase which ceases near the peak time of the *GOES* soft X-ray flare. Sterling et al. (1997) plotted *GOES* soft X-ray flux and hard X-ray flux from HXT for several flares, and found that the *GOES* flux peaked close to the time of the last detectable hard X-ray burst in several events (see Figs. 2e, 3e, 5e, 6e, and 7e of Sterling et al. 1997). This suggests that the deceleration we observe here in Figure 3a corresponds to the deceleration of CMEs discussed by Zhang et al. (2001).

We thank K. Shibata for suggesting the normalized representation of the filament height as a function of time, and we thank D. M. Zarro for software assistance. Both authors were supported by funding from NASA's Office of Space Science through the Solar Physics Supporting Research and Technology Program and the Sun-Earth Connection Guest Investigator Program. *TRACE* is a NASA small explorer project. *Yohkoh* is a mission of the Institute of Space and Astronautical Sciences (Japan), with participation from the US and UK. We thank the Kitt Peak Observatory for providing access to magnetograms.

REFERENCES

Alexander, D., Harra-Murnion, L. K., Khan, J. I., Matthews, S. A. 1998, ApJ, 494, 235

Antiochos, S. K. 1998, ApJ, 502, L181

Antiochos, S. K., DeVore, C. R., & Klimchuk, J. A. 1999, ApJ, 510, 485

Chen, P., & Shibata, K. 2000, ApJ, 545, 524

Fishman, G. J., et al. 1989, in Proc. Gamma-Ray Observatory Science Workshop, ed. W. N. Johnson (Greenbelt: GSFC), 2

Handy, B. N., Bruner, M. E., Tarbel, T. D., Title, A. M., Wolfson, C. J., Laforge, M. J., & Oliver, J. J. 1998, Sol. Phys., 187, 29

Harmon, B. A., et al., ApJS, 138, 149

Harrison, R. A. 1986, A&A, 162, 283

Heyvaerts, J., Priest, E. R., & Rust, D. M. 1977, ApJ, 216, 123

Kahler, S. W., Moore, R. L., Kane, S. R., & Zirin, H. 1988, Sol. Phys., 328, 824

Lin, J., Forbes, T. G., & Isenberg, P. A. 2001, J. Geophys. Res., 106, 25053

Moore, R. L., and LaBonte, B. 1980, in Proc. Symp. on Solar and Interplanetary Dynamics, Reidel, Boston, 207

Moore, R. L., & Roumeliotis, G. 1992, in Eruptive Solar Flares, ed. Z. Svestka, B. V. Jackson, & M. E. Machado (Berlin: Springer), 69

Moore, R. L., Sterling, A. C., Hudson, H. S., & Lemen, J. R. 2001, ApJ, 552, 833

Rust, D. M. 1976, Phil. Trans. Rol. Soc. London, A, 281, 427

Sterling, A. C., Hudson, H. S., Lemen, J. R., Zarro, D. A. 1997, ApJS, 110, 115

Sterling, A. C., & Moore, R. L. 2003, ApJ, 599, 1418

Sterling, A. C., & Moore, R. L. 2004a, ApJ, 602, 1024

Sterling, A. C., & Moore, R. L. 2004b, ApJ, 613, 1221

Sturrock, P. A. 1989, Solar Phys., 121, 387

Tanaka, K., & Zirin, H. 1985, ApJ, 299, 1036

Tandberg-Hanssen, E., Martin, S. F., & Hansen, R. T. 1980, Sol. Phys., 65, 357

Tsuneta, S., et al. 1991, Sol. Phys., 136, 37

Zhang, J., Dere, K. P., Howard, R. A., Kundu, M. R., & White, S. M. 2001, ApJ, 559, 452

Fig. 1.— *TRACE* 195 Å images of the 1998 July 11 filament eruption. White arrows point to the top of the erupting loop-shaped filament in each panel; (a) before filament upward movement starts, (b) during the filament's slow-rise phase, (c) and (d) during the fast-rise phase. Boxes mark regions used to generate lightcurves of Fig. 3 below, with box 1 covering the location of primary flare brightenings, box 2 at the location of early pre-eruption brightenings in (b) and also the location of flare ribbons at later times (c and d), box 3 at the location of a secondary remote brightening, and box 4 at a location of virtually no activity taken to represent background intensity fluctuations. North is up and West is to the right in these and other solar images in this paper.

Fig. 2.— *TRACE* 1600 Å images of the 1998 July 11 filament eruption, with times in each panel near the times in the corresponding panels of Fig. 1, and the boxes at the same locations as those of Fig. 1. Axes ranges are the same as in Fig. 1, but the FOV is different from the 195 Å images resulting in the blank areas at the top and on the right of each panel.

Fig. 3.— Time profiles of filament height, velocity, and acceleration, and of various flare emissions. (a) Curve labeled "height" shows the proper motion displacement of the filament top in the plane of the image in Fig. 1 as a function of time, where error bars represent upper and lower limits for estimates of the filament location; these heights are relative to an arbitrary point on the solar disk along the axis of the filament's motion, with initial height set to 20,000 km. Filament velocity values are calculated by taking time derivatives of the height values smoothed over five points. Acceleration is the derivative of the velocity curve; maximum acceleration is 1.0 km s^{-2} at 04:35 UT and minimum is -0.7 km s^{-2} at 04:37 UT. BATSE hard X-rays cover approximately 30—60 keV, and the Yohkoh HXT data cover approximately 14 — 23 keV; both hard X-ray fluxes are plotted on an arbitrary scale. (b) Thicker lines are *TRACE* 195 Å image light curves derived from boxes in Fig. 1, where the label numbers correspond to the Fig. 1 box labels. Values for the intensities are on an arbitrary scale, and stretched to fit on the same plot; therefore the relative timings of the intensity changes and the variations with time of each lightcurve are meaningful, but the relative intensity levels among different lightcurves are arbitrary. Thinner lines show *TRACE* 1600 Å flux values from the corresponding box regions, with the curves normalized so that the maximum and minimum values match corresponding points in the 195 Å curves. Stars show the ratio of intensities in soft X-rays from SXT AlMg images between box 2 and the rest of the active region (consisting of the intensities of boxes 1, 3, and 5, minus the intensity of box 2, where the boxes are as indicated in Figs. 1, 2, and 4) at four times, but the leftmost star (with leftward-pointing arrow) is actually at 04:07:10 UT, but plotted at 04:11 UT for convenience.

Fig. 4.— (a) Kitt Peak magnetogram of the eruption region scanned from between 16:15 and 17:10 UT on 1998 July 9, with red and blue contours representing positive and negative flux, respectively. Red and blue contours are of magnitude 50, 100, and 200 G, while orange and turquoise contours show stronger-field regions of magnitude 400, 600, and 1000 G. The magnetogram has been rotated so that in subsequent panels the contours of (a) register with: (b) a *TRACE* 195 Å image from 04:23:55 UT, (c) a *TRACE* 1600 Å image from 04:33:55 UT, and (d) an SXT AlMg image from 04:24:06 UT, all on 1998 July 11. In (c), arrow 1 points to the prominent negative spot, arrows 2 and 3 indicate a newly-emerged bipole, arrows 4—6 show concentrations of positive flux that help form a neutral line with the negative fields immediately to the west, and arrow 7 shows the eruption-time brightenings of box 3 in Figures 2c and 2d. Boxes in (d) correspond to those of Fig. 1a, with one additional box, box 5, labeled here. Images in (b) and (d) are near the time of the peak of the pre-eruption brightening in *TRACE* 195 (Fig. 3b).

Fig. 5.— Close up of the *TRACE* 1600 Å images of the erupting region (a) prior to and (b and c) during the time of the filament's slow rise, and (d—f) early in the fast eruption. The white box in (b) is box 2 of Figs. 1 and 2. A feature brightens at the location of that box between the time of the images in panels (a) and (b), and continues to evolve though (d). Flare ribbons, identified by arrows r1 — r6, appear in (e), and continue to evolve through the time of (f). The magnetogram of Fig. 4 is overlaid onto (c) and (f), with arrows 2 and 3 in (f) the same as those of Fig. 4c.

Fig. 6.— As in Fig. 5, but for *TRACE* 195 Å, where again the white box in (b) is box 2 of Figs. 1 and 2 and flare ribbons are again apparent and identified by arrows r1 — r6 in (e). The initial pre-eruption brightening appears beneath the filament during its slow-rise phase in (b) and (c). The top of the filament has left the field of view during its fast-rise phase in (e) and (f).

Fig. 7.— Schematic representation of inferred magnetic geometry of the eruption region, based on the Kitt Peak magnetogram of Fig. 4 and the locations of flare ribbons and other features in Figs. 5 and 6; regions R1—R6 correspond to the ribbon locations in those figures. The black dashed line indicates the primary magnetic inversion line, with plus (+) and minus (−) polarity regions indicated; the kink in the inversion line between regions R1 and R2 represents our guess of the effect on the neutral line of the flux which emerged about 35 hrs prior to eruption. Thick black solid lines indicate representative field lines which show up as coronal loops. Prior to eruption the filament resided on Loop 1. We suggest that an initial period of slow reconnection between pre-existing sheared loops beneath the filament, represented by blue and red lines, results in formation of new loops, represented by the solid and dashed green lines; it is a continuum of solid and dashed green lines that we see as the feature in box 2 of Figs. 5b and 6b. Eventually this process leads to eruption of the filament.

Fig. 8.— Normalized time development of the filament eruption and hard X-ray burst. The thick profile is the filament height as a function of time as in Fig. 3a, but where the height is normalized to an Alfven scale length, L_A, of the system (which we take to be the distance of the separation of the filament footpoints) and the elapsed time, t, is normalized to the corresponding Alfven travel time, τ_A, of the system. Zero height and zero time are arbitrarily set, and the thin horizontal line is at height zero. The thin profile is velocity, also in normalized units. BATSE hard X-ray fluxes Fig. 3a are also plotted at the corresponding normalized time.

Fig. 9.— Height of the center of a flux tube (h) and rate of magnetic reconnection (R) as functions of time as predicted in the reconnection eruption model due to Chen & Shibata (2000). (This figure is Fig. 6 in their paper, and represents results for case A of the model discussed in that paper.) Units for height and time are the same as in Fig. 8, for the parameters used by Chen & Shibata.

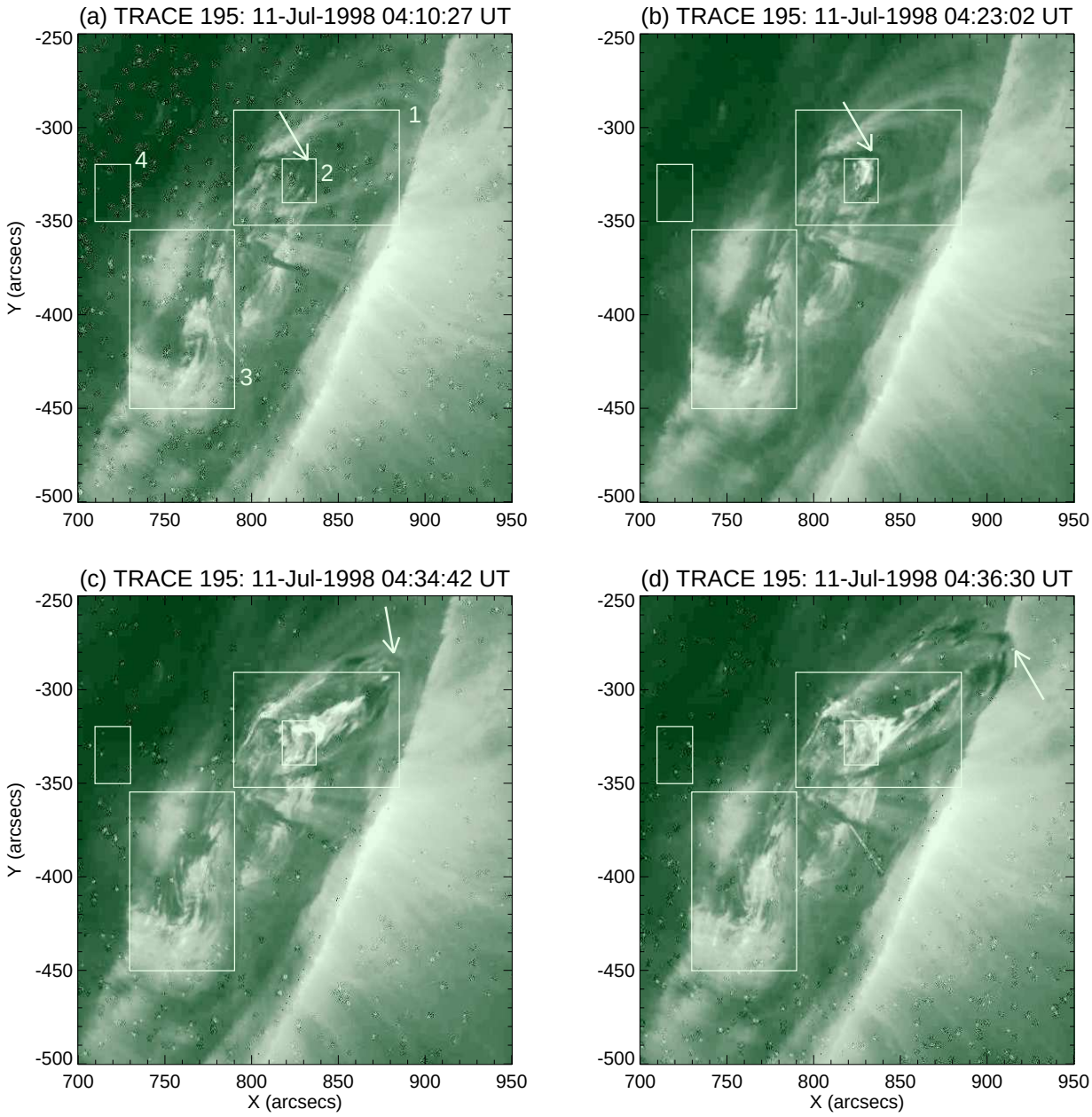
(a) TRACE 195: 11-Jul-1998 04:10:27 UT
(b) TRACE 195: 11-Jul-1998 04:23:02 UT
(c) TRACE 195: 11-Jul-1998 04:34:42 UT
(d) TRACE 195: 11-Jul-1998 04:36:30 UT
1
2
3
4
Y (arcsecs)
X (arcsecs)
-250
-300
-350
-400
-450
-500
700
750
800
850
900
950

Fig. 1

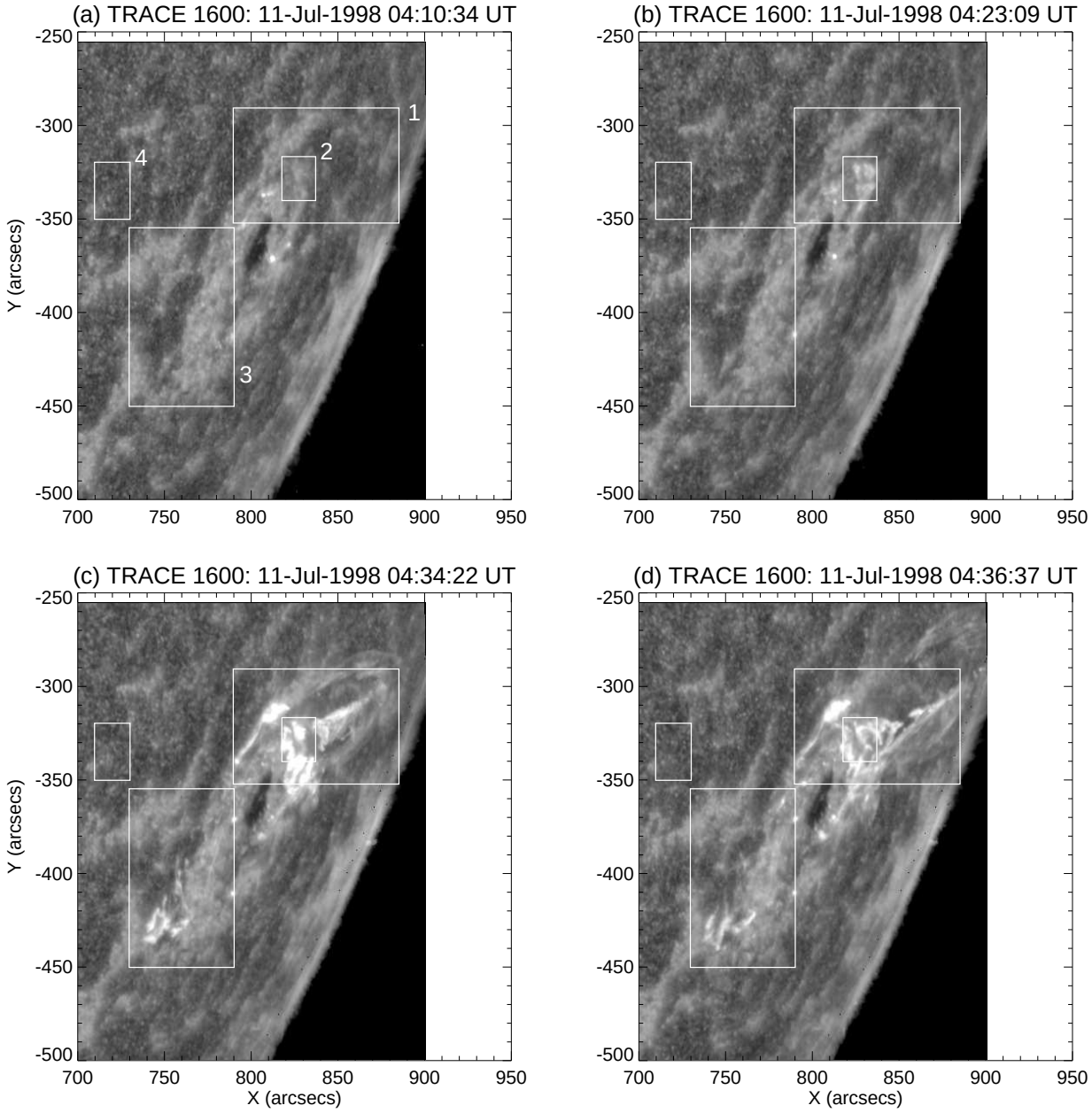
(a) TRACE 1600: 11-Jul-1998 04:10:34 UT
(b) TRACE 1600: 11-Jul-1998 04:23:09 UT
(c) TRACE 1600: 11-Jul-1998 04:34:22 UT
(d) TRACE 1600: 11-Jul-1998 04:36:37 UT
1
2
3
4
Y (arcsecs)
X (arcsecs)
-250
-300
-350
-400
-450
-500
700
750
800
850
900
950

Fig. 2

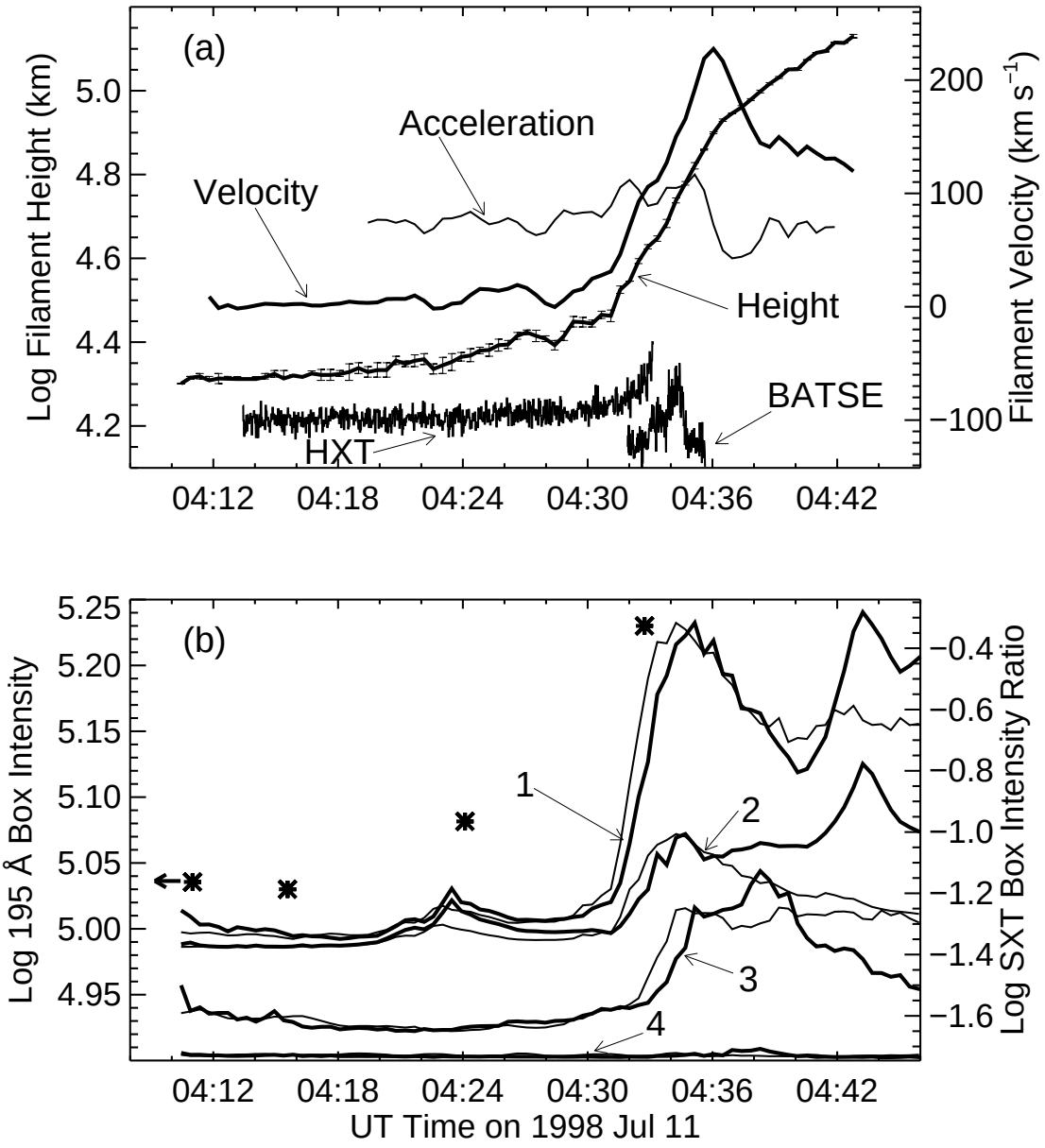
(a)
Log Filament Height (km)
5.0
4.8
4.6
4.4
4.2
Filament Velocity (km s^{-1})
200
100
0
−100
Acceleration
Velocity
Height
BATSE
HXT
04:12
04:18
04:24
04:30
04:36
04:42
(b)
Log 195 Å Box Intensity
5.25
5.20
5.15
5.10
5.05
5.00
4.95
Log SXT Box Intensity Ratio
−0.4
−0.6
−0.8
−1.0
−1.2
−1.4
−1.6
1
2
3
4
04:12
04:18
04:24
04:30
04:36
04:42
UT Time on 1998 Jul 11

Fig. 3

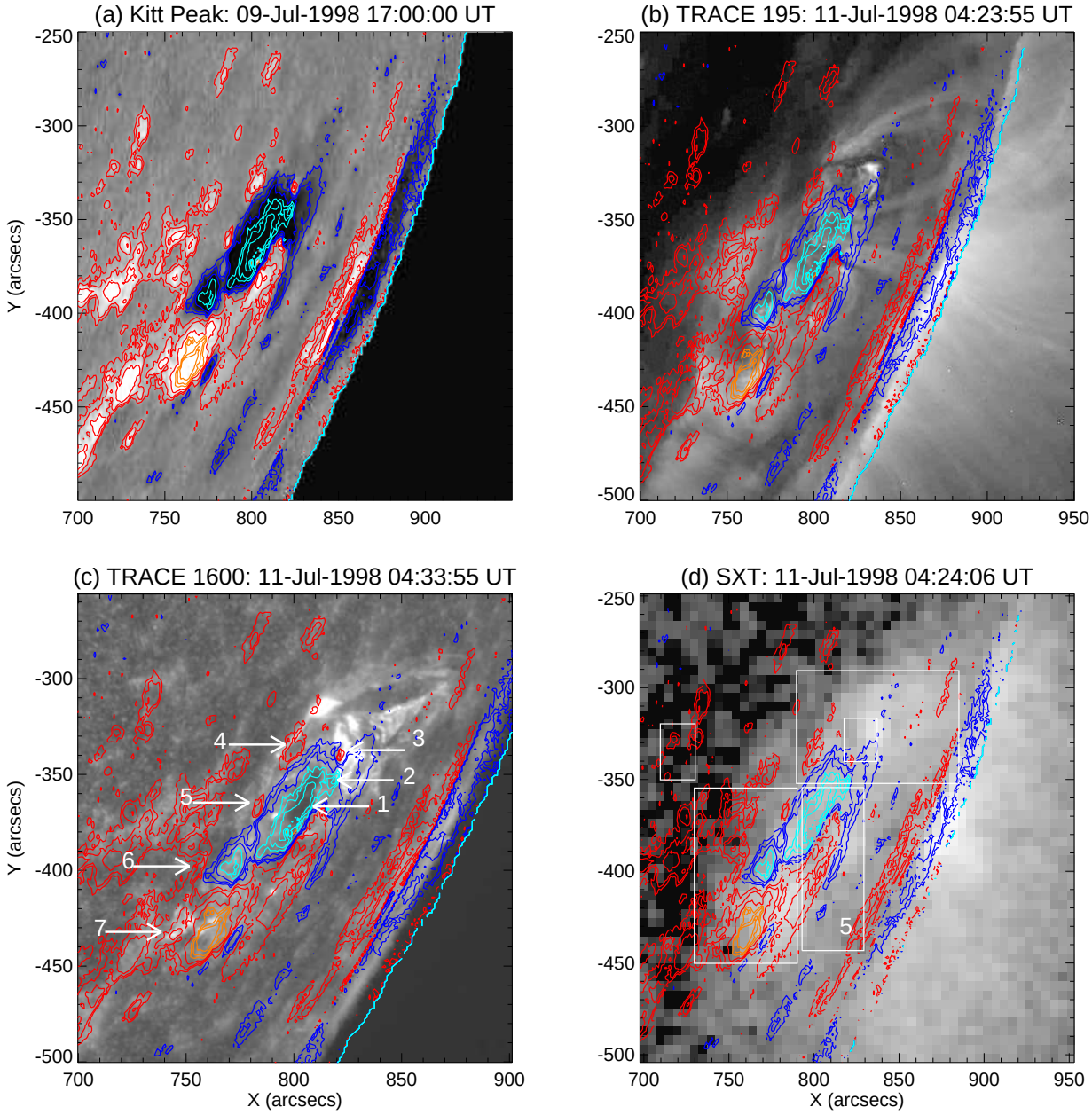
(a) Kitt Peak: 09-Jul-1998 17:00:00 UT
(b) TRACE 195: 11-Jul-1998 04:23:55 UT
(c) TRACE 1600: 11-Jul-1998 04:33:55 UT
(d) SXT: 11-Jul-1998 04:24:06 UT
Y (arcsecs)
X (arcsecs)
-250
-300
-350
-400
-450
-500
700
750
800
850
900
950
1
2
3
4
5
6
7

Fig. 4

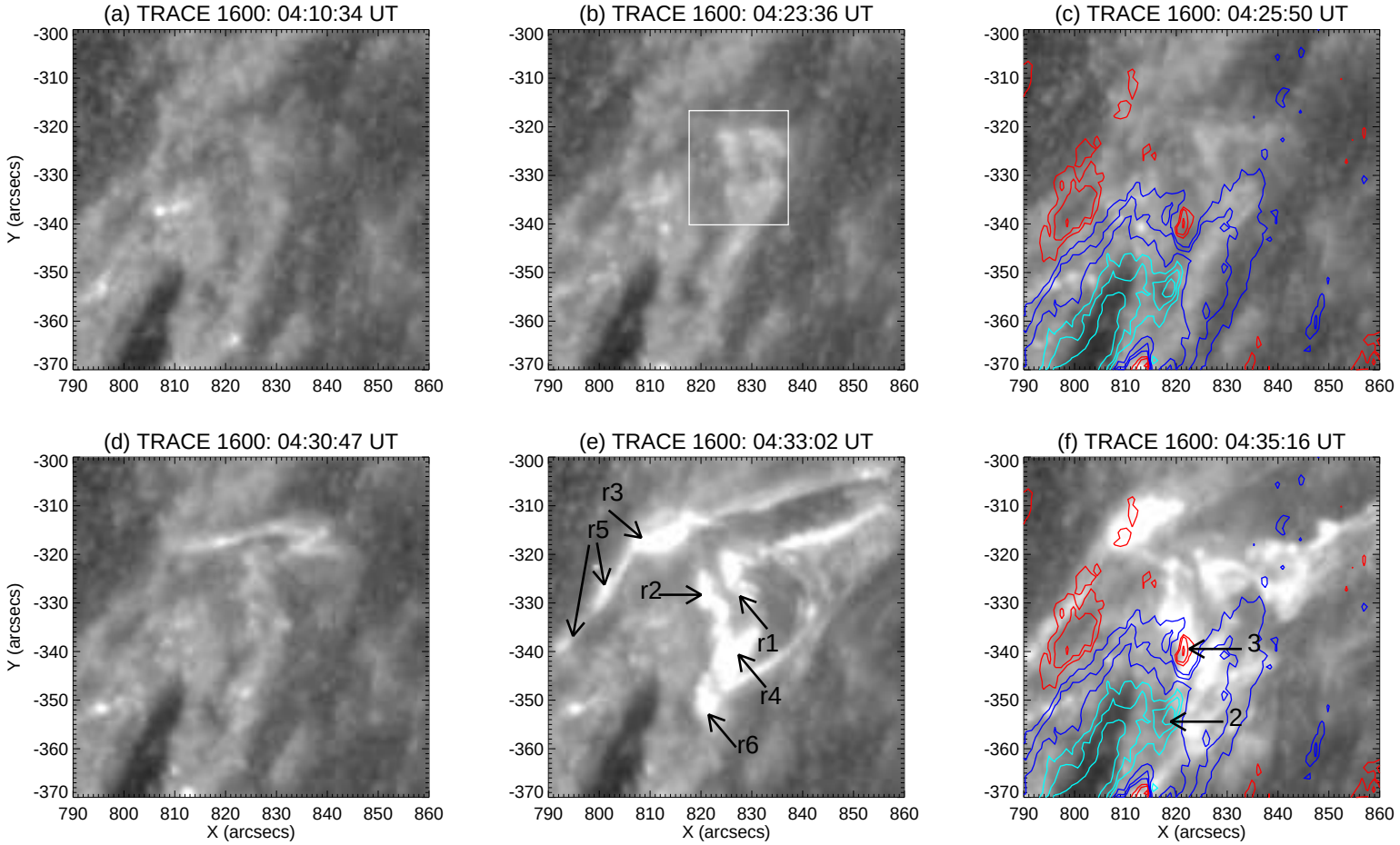
(a) TRACE 1600: 04:10:34 UT
(b) TRACE 1600: 04:23:36 UT
(c) TRACE 1600: 04:25:50 UT
(d) TRACE 1600: 04:30:47 UT
(e) TRACE 1600: 04:33:02 UT
(f) TRACE 1600: 04:35:16 UT
Y (arcsecs)
X (arcsecs)
-300
-310
-320
-330
-340
-350
-360
-370
790
800
810
820
830
840
850
860
r1
r2
r3
r4
r5
r6
2
3

Fig. 5

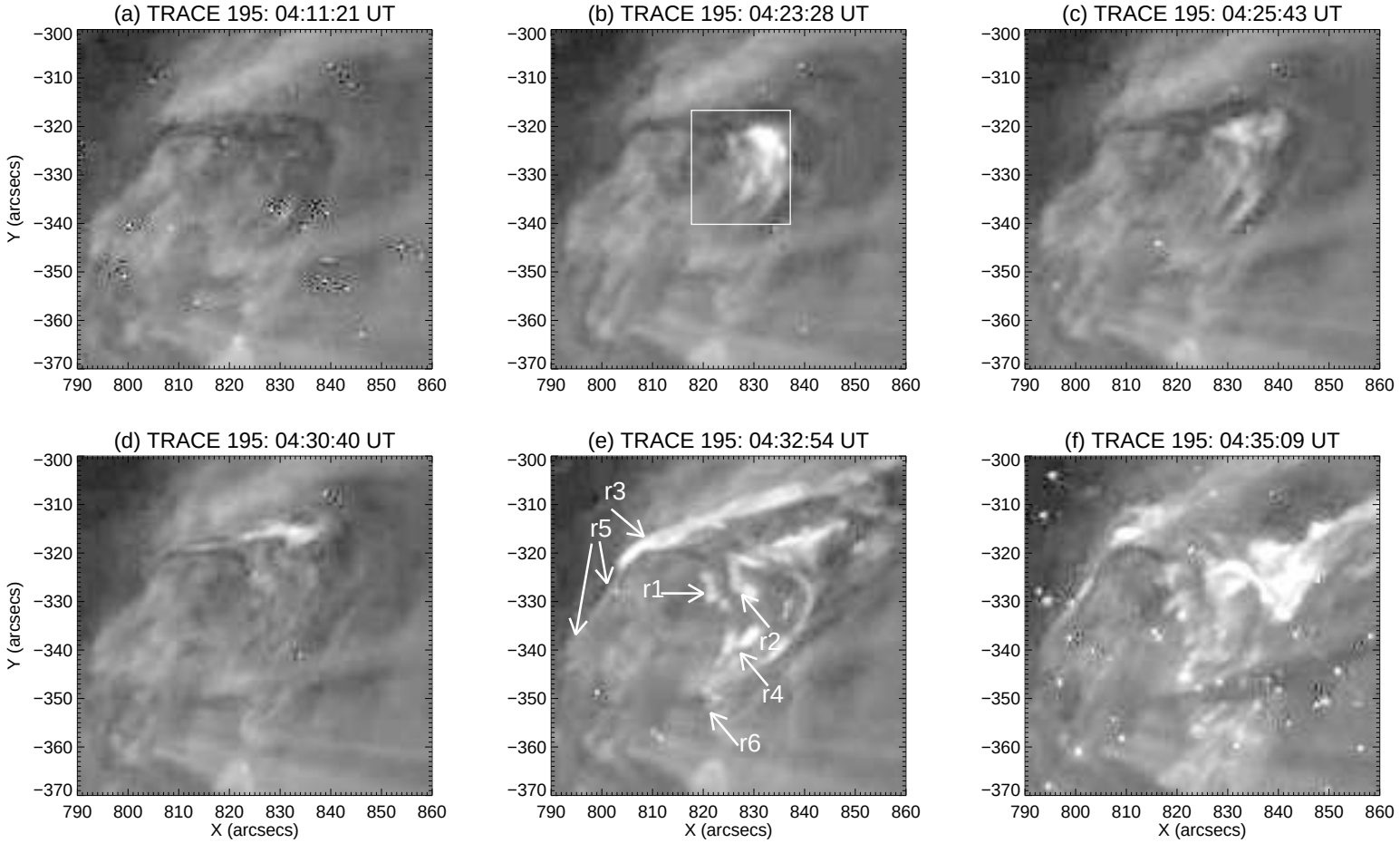
(a) TRACE 195: 04:11:21 UT
(b) TRACE 195: 04:23:28 UT
(c) TRACE 195: 04:25:43 UT
(d) TRACE 195: 04:30:40 UT
(e) TRACE 195: 04:32:54 UT
(f) TRACE 195: 04:35:09 UT
r1
r2
r3
r4
r5
r6
Y (arcsecs)
X (arcsecs)
−300
−310
−320
−330
−340
−350
−360
−370
790
800
810
820
830
840
850
860

Fig. 6

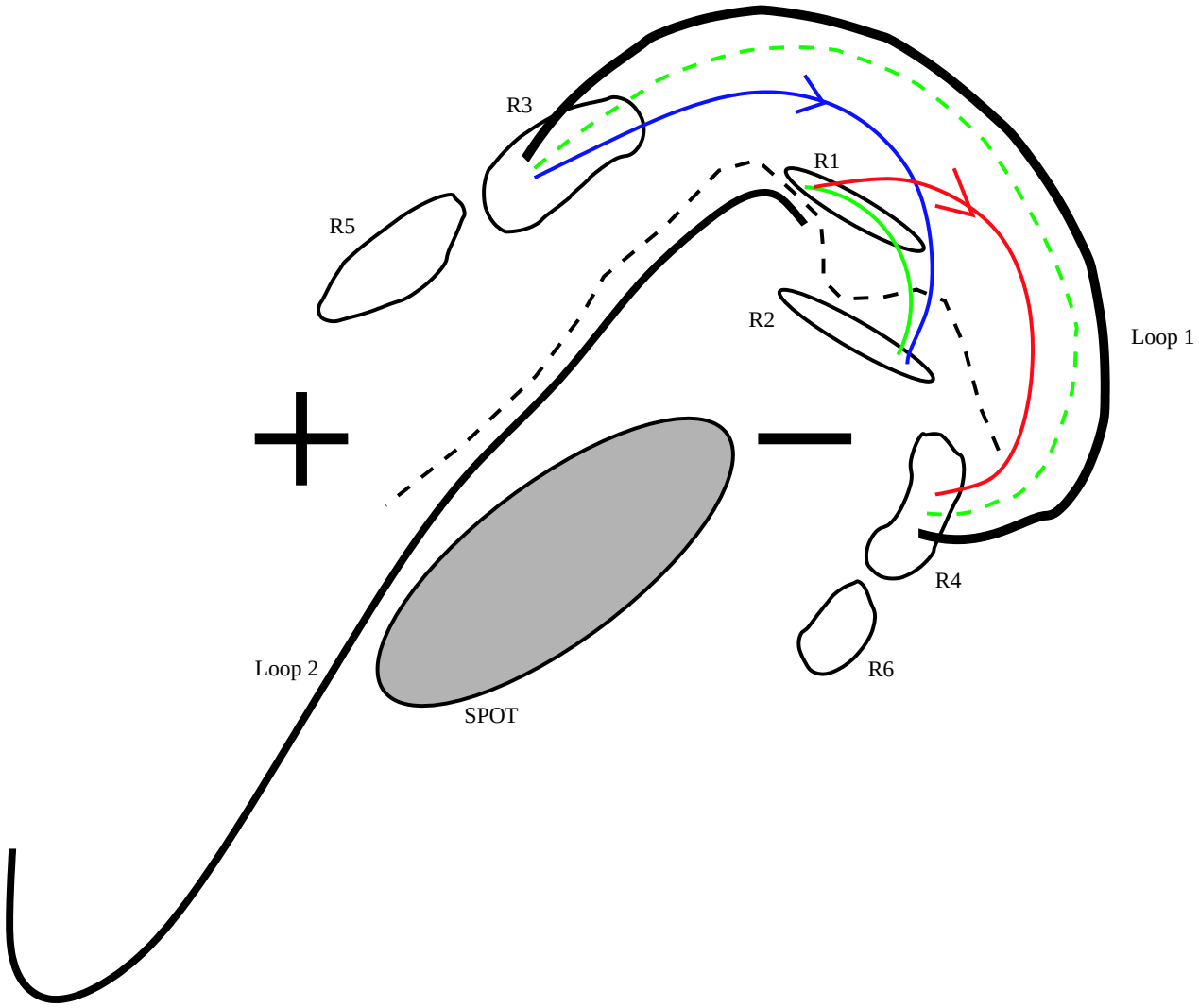

Fig. 7

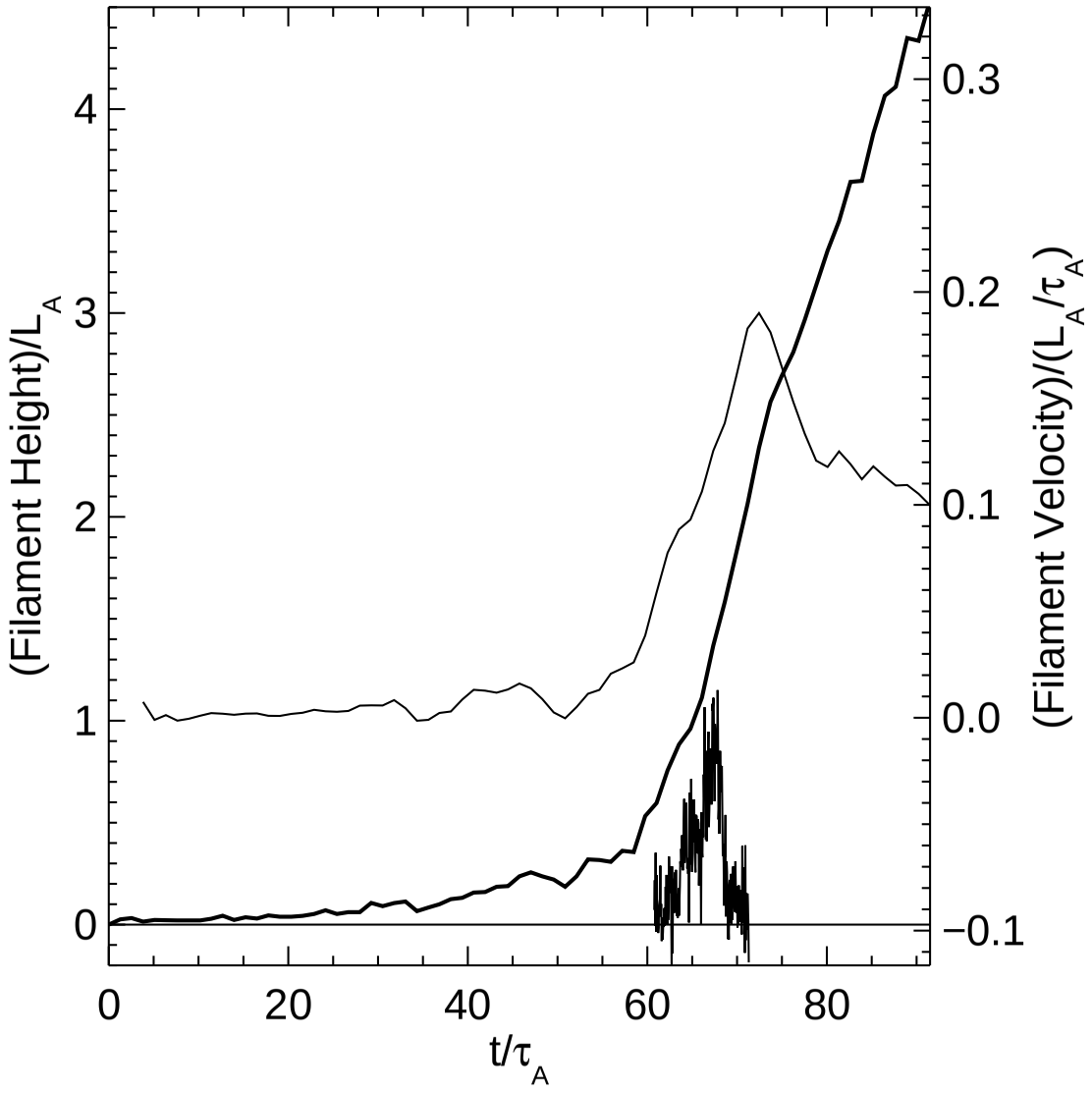
(Filament Height)/L_A
(Filament Velocity)/(L_A/τ_A)
t/τ_A
0
20
40
60
80
0
1
2
3
4
−0.1
0.0
0.1
0.2
0.3

Fig. 8

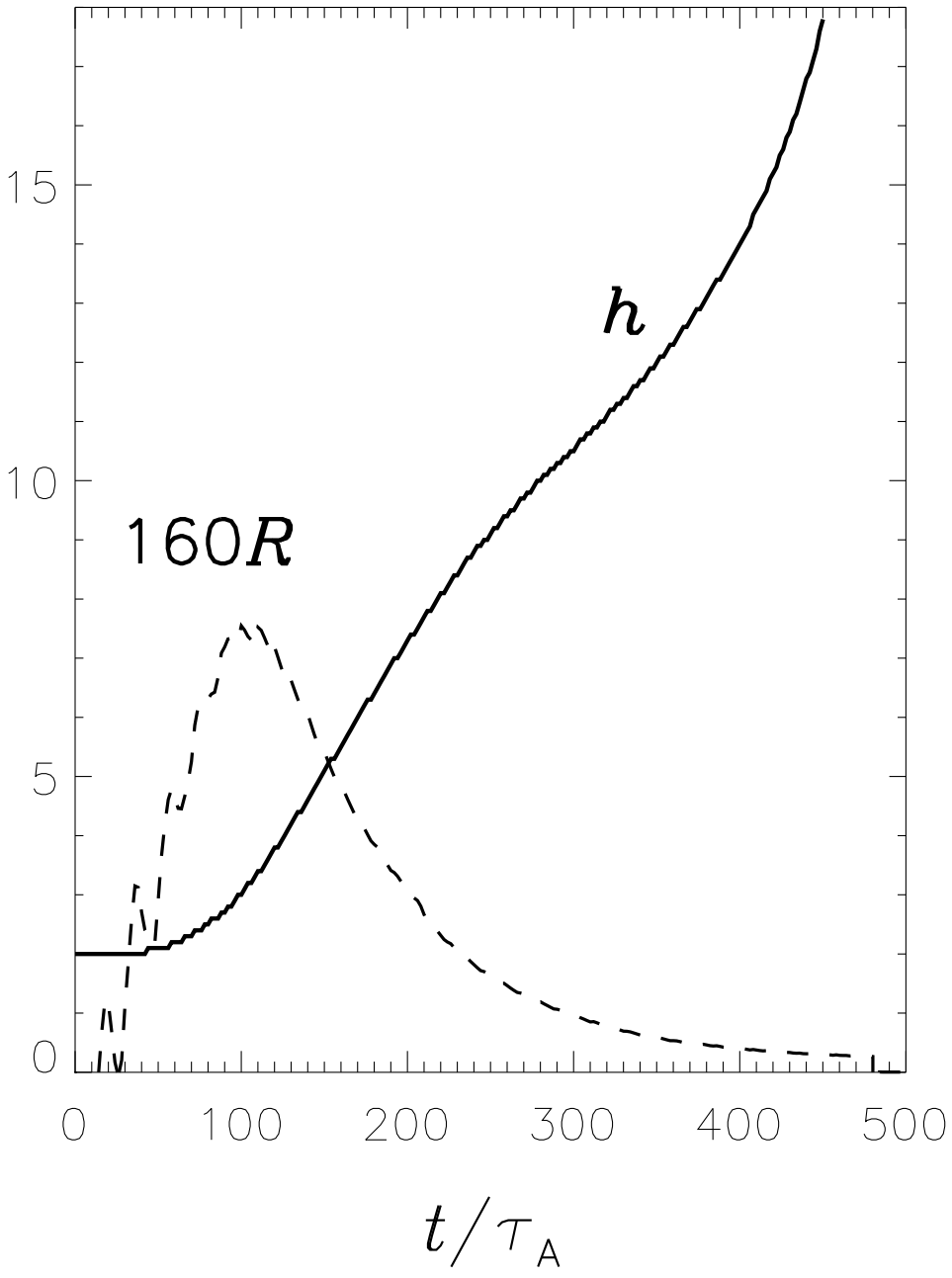

Fig. 9